Supplementary Material:

Polarization Fields: Dynamic Light Field Display using Multi-Layer LCDs

Douglas Lanman[1] Gordon Wetzstein[2] Matthew Hirsch[1] Wolfgang Heidrich[2] Ramesh Raskar[1]
[1]MIT Media Lab [2]University of British Columbia

This document contains additional results, implementation details, and extended evaluations in support of the primary text. Appendix A includes additional images of the prototype construction. Appendix B further documents 3D display performance with polarization-rotating layers and comparisons to light-attenuating layers. Appendix C applies the Jones calculus to model multi-layer, multi-domain LCDs and compares this model to experimental measurements. Pseudocode and additional evaluations of the real-time, GPU-based SART solver are given in Appendix D.

A Construction of the Multi-Layer Display Prototype

Figure S.1: *Photographic documentation of the prototype construction. Four monochrome, off-the-shelf medical LCDs were modified. Polarizing films were removed and electronics repositioned so the panels could be mounted on custom-fabricated frames. The layers are separated by acrylic spacers and illuminated by a uniform backlight.*

B Additional Results for Light Field Display

Figure S.2: *Additional results for the "Buddha" scene, using the "Buddha" model from* `http://graphics.stanford.edu/data/3Dscanrep/`. *Simulated views are compared for polarization-rotating layers (first and second columns) and attenuating layers (fourth and fifth columns). Rows illustrate, from top to bottom: target views, reconstructions using the off-line solver for two, three, and four layers (for the same depth range), and SART reconstructions with two, five, and fifty iterations with four layers. Columns three and six present decomposed layers.*

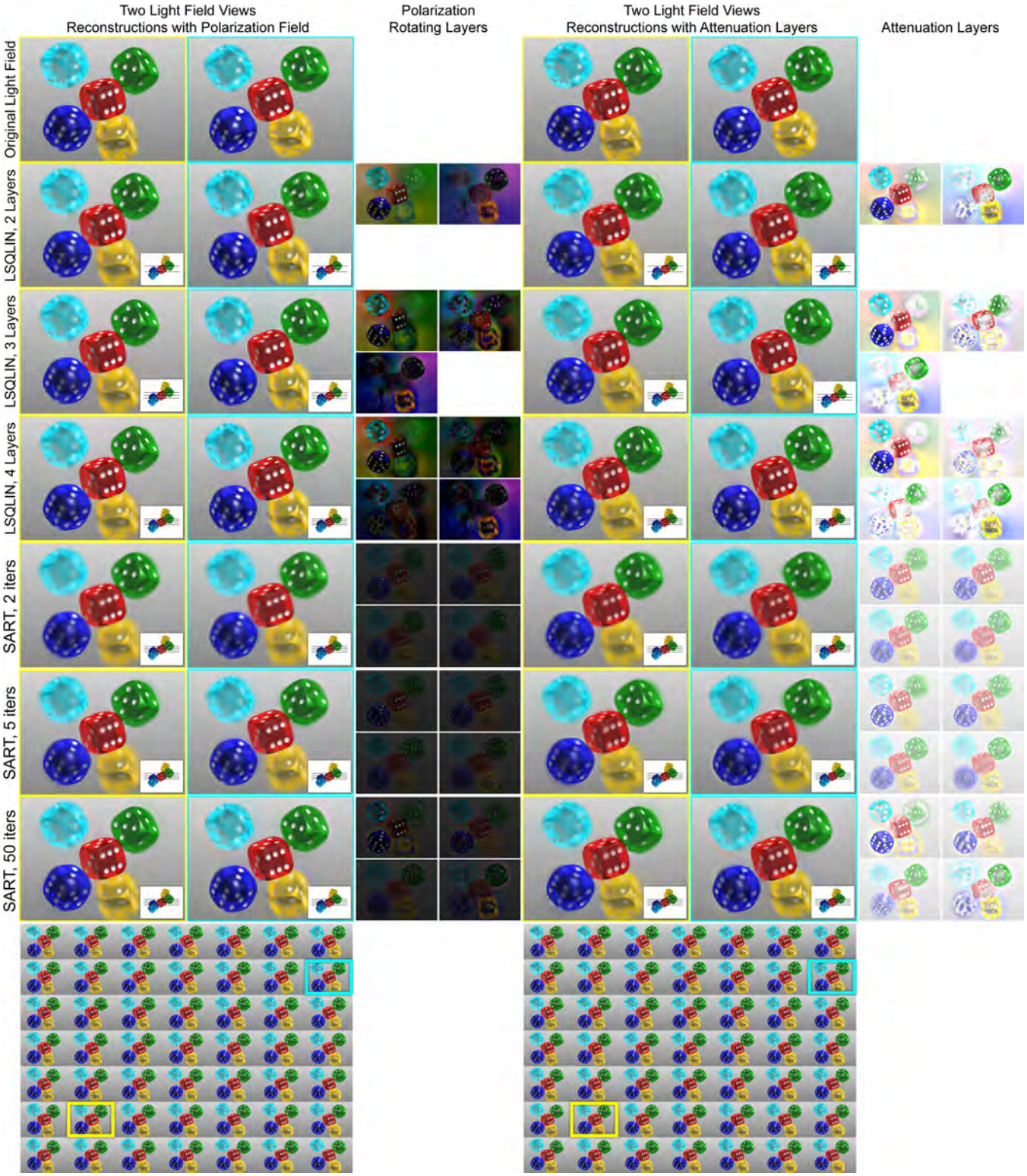

Figure S.3: *Additional results for the "dice" scene, taken from the archive available at* `http://www.layered3d.com`*. The display dimensions and optimization parameters match that of the prototype and correspond with those used in Figure S.2. The light field has a resolution of* 512×384 *spatial samples and* 7×7 *angular samples. The target imagery spans a field of view of* 10 *degrees.*

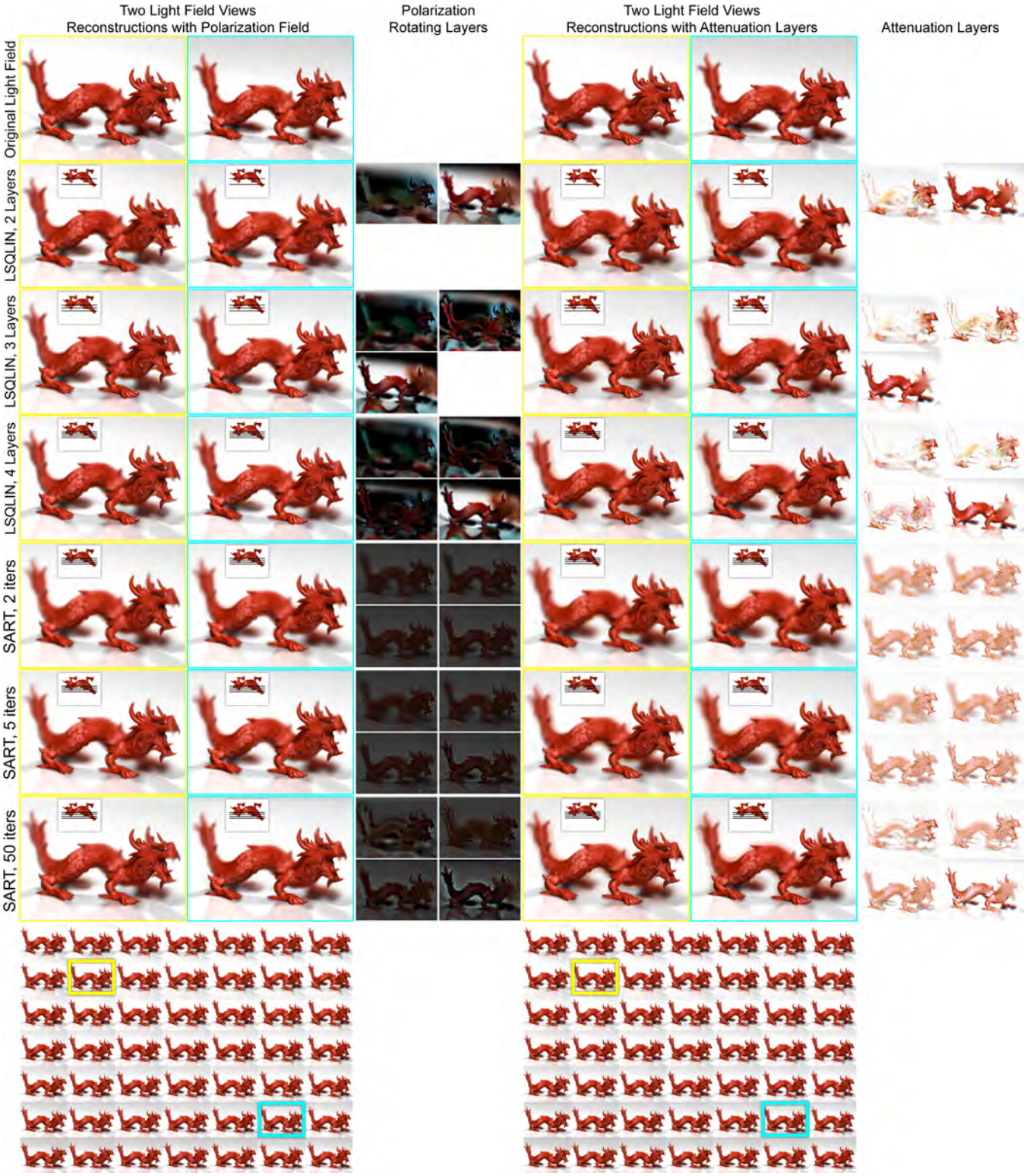

Figure S.4: *Additional results for the "dragon" scene, using the "dragon" model from* `http://graphics.stanford.edu/data/3Dscanrep/`*. The display dimensions and optimization parameters match that of the prototype and correspond with those used in Figure S.2. The light field has a resolution of* 512×384 *spatial samples and* 7×7 *angular samples. The target imagery spans a field of view of* 10 *degrees.*

Figure S.5: *Additional results for the "car" scene, taken from the archive available at* `http://www.layered3d.com`*. The display dimensions and optimization parameters match that of the prototype and correspond with those used in Figure S.2. The light field has a resolution of* 512×384 *spatial samples and* 7×7 *angular samples. The target imagery spans a field of view of* 10 *degrees.*

C Modeling Multi-Layer, Multi-Domain LCDs

This supplementary appendix uses the Jones calculus to model multi-layer, multi-domain LCD panels, expanding on Appendix A of the primary text. We formally assess the deviations of our prototype, which uses four in-plane switching (IPS) LCDs, from the ideal multi-layer polarization rotator implementation by applying the multi-domain LCD model introduced by Date et al. [2005]. In Section C.1 we derive analytic expressions for the normalized intensity emitted by single-layer LCDs containing either one or two domains. These models are compared to experimental measurements, confirming that the panels used in the prototype contain multiple domains. In Section C.2 we derive expressions for the normalized intensity emitted by such multi-layer, multi-domain LCDs. The resulting non-linear image formation model well-approximates artifacts observed with the prototype; yet, this model also prohibits real-time optimization in the manner facilitated by a multi-layer polarization rotator approximation. We conclude by discussing optimal LCD architectures for practical dynamic light field display with minimal artifacts.

C.1 Single-Layer LCDs

The transformation of polarized light due to passage through layered materials is modeled by the Jones calculus [Jones 1941]. In this section we use this formalism to characterize the polarization properties of LCD panels. We assume familiarity with the Jones calculus and recommend Collett [2005] or Yeh and Gu [2009] for a review.

C.1.1 Polarization Rotators

Section 3 of the primary text introduces the polarization rotator model, wherein a single LCD panel is approximated as applying a linear rotation to the incident polarization state. Recall that the Jones matrix $\mathbf{R}(\theta)$, representing a rotation by an angle of θ, is given by the following expression.

$$\mathbf{R}(\theta) = \begin{pmatrix} \cos(\theta) & \sin(\theta) \\ -\sin(\theta) & \cos(\theta) \end{pmatrix} \tag{S.1}$$

Also recall that the Jones matrix $\mathbf{J}(\xi)$, representing a counterclockwise rotation of an optical element by an angle ξ, is given by $\mathbf{R}(-\xi)\,\mathbf{J}\,\mathbf{R}(\xi)$, where $\mathbf{J}$ is the Jones matrix for the unrotated element. Using these facts, we derive the following expression for the normalized intensity $I_{\text{R-1}}(\phi, \xi)$ for a single polarization rotator enclosed by a pair of linear polarizers, as a function of the applied polarization state rotation angle ϕ and the angle ξ between the axes of the front and rear polarizers.

$$I_{\text{R-1}}(\phi, \xi) = I_0 \left\| \left(\mathbf{R}(-\xi) \begin{pmatrix} 1 & 0 \\ 0 & 0 \end{pmatrix} \mathbf{R}(\xi) \right) \mathbf{R}(-\phi) \begin{pmatrix} 1 \\ 0 \end{pmatrix} \right\|^2 = I_0 \cos^2(\phi - \xi) \tag{S.2}$$

Here, the vector norm is defined such that $\|(E_x \;\; E_y)^\top\| = \sqrt{|E_x|^2 + |E_y|^2}$. Note the rear polarizer (closest to the backlight) is the assumed to be horizontally aligned, whereas the front polarizer (i.e., the analyzer) is freely rotated. By convention, we assume the polarization rotator applies a counterclockwise rotation. For crossed polarizers (i.e., $\xi = \pi/2$), Equation S.2 yields $I_{\text{R-1}}(\phi, \pi/2) = I_0 \sin^2(\phi)$, confirming Malus' law (Equation 1 in the primary text).

C.1.2 Single-Domain LCDs

As described by Yeh and Gu [2009], the Jones matrix modeling an LCD panel depends on the underlying architecture, with specific derivations presented for twisted nematic (TN), in-plane switching (IPS), and vertical alignment (VA) variants. Yet, as characterized by Date et al. [2005], all such panels are fundamentally retardation-based displays; as such, they can be generally represented by a Jones matrix model corresponding to a *rotated wave plate*. Recall that the Jones matrix $\mathbf{J}_{\text{WP}}(\psi)$, representing a wave plate (i.e., a phase retarder), is given by

$$\mathbf{J}_{\text{WP}}(\psi) = \begin{pmatrix} 1 & 0 \\ 0 & e^{-i\psi} \end{pmatrix}, \tag{S.3}$$

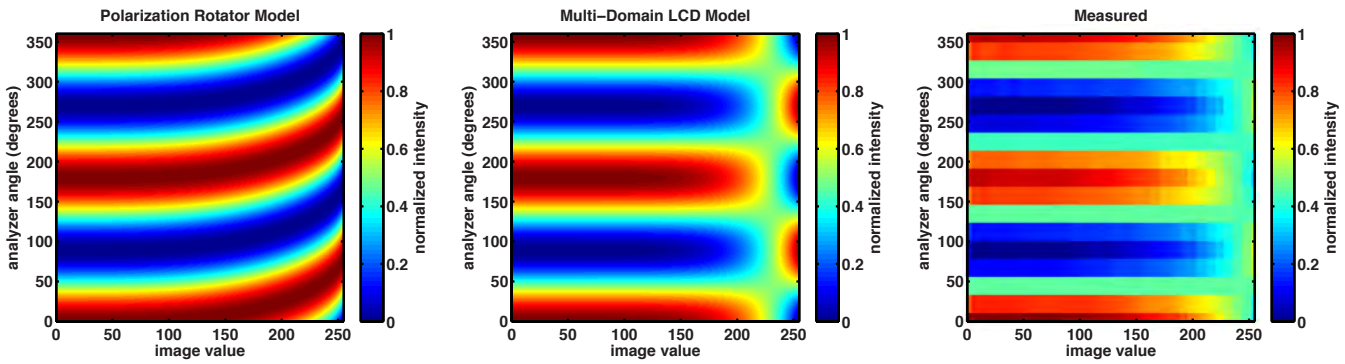

Figure S.6: *Comparing single-layer LCD models to experimental measurements. (Right) Normalized intensity for a Barco E-2320 PA panel as a function of image value v and analyzer angle ξ. A horizontally-aligned linear polarizer was placed between the backlight and the panel. A second polarizer (i.e., the analyzer) was affixed to a rotation mount and placed between the front of the LCD and a photometer. The normalized intensities predicted under the single-domain model (Equation S.6) and the two-domain model (Equation S.7) are shown on the left and in the middle, respectively. Note that the multi-domain model accurately predicts experimental measurements. Yet, also note that the polarization rotator model (equivalent to the profile on the left) provides an accurate approximation for small image values, such as those predominantly used by multi-layer decompositions in Figures S.2–S.5.*

where $\psi/2$ is the phase shift induced along the horizontal (fast) and the vertical (slow) axes [Collett 2005]. Similarly, the Jones matrix $\mathbf{J}_{\text{P}}(\alpha, \psi)$, representing a wave plate rotated by an angle α, is given by the following expression.

$$\mathbf{J}_{\text{P}}(\alpha, \psi) = \mathbf{R}(-\alpha)\, \mathbf{J}_{\text{WP}}(\psi)\, \mathbf{R}(\alpha) = \begin{pmatrix} \cos^2(\alpha) + e^{-i\psi} \sin^2(\alpha) & (1 - e^{-i\psi}) \cos(\alpha) \sin(\alpha) \\ (1 - e^{-i\psi}) \cos(\alpha) \sin(\alpha) & e^{-i\psi} \cos^2(\alpha) + \sin^2(\alpha) \end{pmatrix} \tag{S.4}$$

Note that, when representing an LCD panel as a rotated wave plate, α corresponds to the angle of the liquid crystal director. Date et al. [2005] explain that LCD designers typically select $\psi = \pi$ to maximize transmittance. Under this assumption, a general LCD panel is modeled as a *rotated half-wave plate*, with a Jones matrix $\mathbf{J}_{\text{HWP}}(\alpha)$ given by:

$$\mathbf{J}_{\text{HWP}}(\alpha) = \mathbf{J}_{\text{P}}(\alpha, \pi) = \begin{pmatrix} \cos(2\alpha) & \sin(2\alpha) \\ \sin(2\alpha) & -\cos(2\alpha) \end{pmatrix}. \tag{S.5}$$

Note the similarity between the Jones matrices representing a rotated half-wave plate (Equation S.5) and a polarization rotator (Equation S.1). Compared to a polarization rotator, a rotated half-wave plate acts as a *pseudo-rotator*: reversing the polarization state and doubling the rotation angle [Collett 2005]. Under this model, a single-domain LCD panel (e.g., a conventional TN panel) can be approximated as a spatially-controllable rotated half-wave plate. Similar to Equation S.2, the following expression characterizes the normalized intensity $I_{\text{HWP-1-1}}(\alpha, \xi)$ for a rotated half-wave plate enclosed by a pair of linear polarizers, where α denotes the liquid crystal director angle (i.e., the fast axis of the retarder) and ξ is the angle between the front and rear polarizers.

$$I_{\text{HWP-1-1}}(\alpha, \xi) = I_0 \left\| \left(\mathbf{R}(-\xi) \begin{pmatrix} 1 & 0 \\ 0 & 0 \end{pmatrix} \mathbf{R}(\xi) \right) \mathbf{J}_{\text{HWP}}(\alpha) \begin{pmatrix} 1 \\ 0 \end{pmatrix} \right\|^2 = I_0 \cos^2(2\alpha - \xi) \tag{S.6}$$

For $\alpha = \phi/2$, the right-hand sides of Equations S.2 and S.6 are equal. Thus, under this model, single-layer, single-domain LCDs can be operated equivalently to spatially-controllable polarization state rotators.

C.1.3 Multi-Domain LCDs

Our prototype uses an in-plane switching LCD (i.e, Barco E-2320 PA). Pixels in such panels contain more than one liquid crystal *domain*, each of which can (potentially) act independently on the incident polarization state. However,

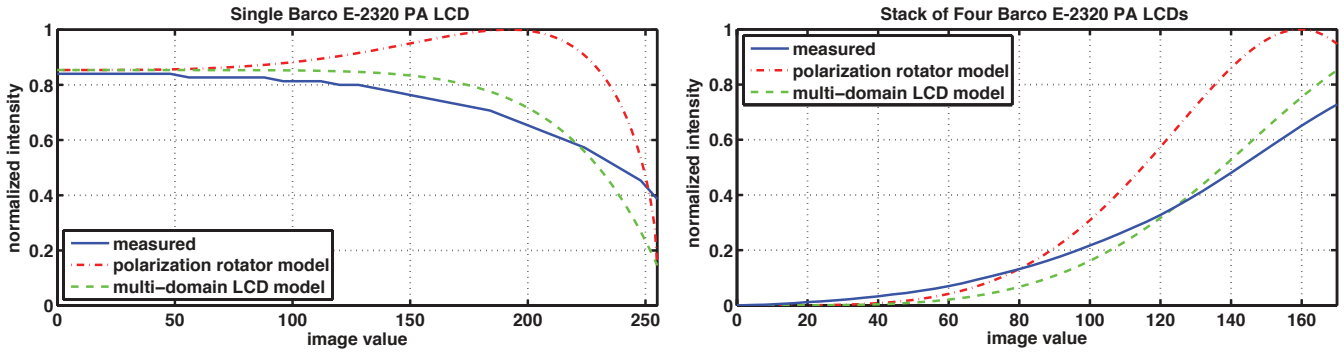

Figure S.7: *Assessing model accuracy for single-layer and four-layer LCDs. (Left) Plots of the normalized intensity emitted by a single LCD panel when the front polarizer is rotated, in the counterclockwise direction, by an angle of* 22.5 *degrees. (Right) Plots of the normalized intensity emitted by the four-layer prototype when each layer displays an identical image value* v*. In both cases, the measurements are more accurately predicted by the multi-domain LCD model (Equations S.7 and S.17), rather than the polarization rotator model (Equation S.10). Yet, similar to Figure S.6, the polarization rotator model remains an accurate approximation for small rotation angles, particularly for the four-layer LCD configuration (e.g., overestimating the output image brightness for larger input image values).*

following the model proposed by Date et al. [2005], we assume each IPS pixel is divided into two domains. Each domain i is approximated by a rotated half-wave plate with Jones matrix $\mathbf{J}_{\text{HWP}}(\alpha^{(i)})$, where the two domains have liquid crystal directors oriented in opposite directions (i.e., $\alpha^{(1)} = -\alpha^{(2)} = \alpha$). Thus, the following expression describes the normalized intensity $I_{\text{HWP-1-2}}(\alpha, \xi)$ for a two-domain IPS panel enclosed by a pair of linear polarizers.

$$I_{\text{HWP-1-2}}(\alpha,\xi) = \frac{I_0}{2}\sum_{i=1}^{2}\left\|\left(\mathbf{R}(-\xi)\begin{pmatrix}1 & 0\\ 0 & 0\end{pmatrix}\mathbf{R}(\xi)\right)\mathbf{J}_{\text{HWP}}\left(\alpha^{(i)}\right)\begin{pmatrix}1\\0\end{pmatrix}\right\|^2 = I_0\left(\frac{\cos^2(2\alpha+\xi)+\cos^2(2\alpha-\xi)}{2}\right) \quad \text{(S.7)}$$

Note that, when enclosed by a pair of crossed linear polarizers (i.e., $\xi = \pi/2$), both domains yield a transmittance function identical to Equation S.6 (i.e., $I_{\text{HWP-1-2}}(\alpha, \pi/2) = I_{\text{HWP-1-1}}(\alpha, \pi/2)$). Thus, having two domains does not alter the transmittance properties compared to a single-domain architecture. In practice, IPS panels with multiple domains exhibit improved field of view, while achieving consistent color and contrast [Yeh and Gu 2009].

Equations S.2, S.6, and S.7 were used to characterize the Barco E-2320 PA panels. A horizontally-aligned linear polarizer was placed between the backlight and the panel. A second polarizer (i.e., the analyzer) was affixed to a rotation mount and placed between the front of the LCD and a photometer. Equation 10 from the primary text was used to convert between the liquid crystal director angle $\alpha \in [0, \pi/4]$ and the image value $v \in [0, 255]$, such that

$$v(\alpha) = \lfloor 255 \sin^{2/\gamma}(2\alpha) + 0.5 \rfloor, \quad \text{(S.8)}$$

where γ is the estimated gamma value. As shown in Figure S.6, a set of photometer measurements were recorded as the image value v varied over $[0, 255]$ and as the analyzer was rotated from 0 to 360 degrees. From these measurements we confirm that the Barco E-23020 PA panel contains multiple domains, exhibiting a close similarity to the two-domain model given by Equation S.7. A subset of these measurements are shown, for an analyzer angle of 22.5 degrees, on the left of Figure S.7. We further observe that Equation S.7 makes an important prediction that can be used to distinguish between single-domain and multi-domain LCDs: when the analyzer is rotated by 45 degrees, the emitted intensity is half of the maximum value (i.e., $I_{\text{HWP-1-2}}(\alpha, \pi/4) = 1/2$). In other words, an arbitrary image displayed on a multi-domain IPS panel will be converted to a uniform intensity when the front polarizer is rotated by 45 degrees. This effect is observed with the prototype, again confirming our panels contain more than one domain.

C.2 Multi-Layer LCDs

This section applies the Jones calculus to analyze multi-layer LCDs. First, we characterize ideal multi-layer polarization rotators. Second, we consider multi-layered, single-domain LCDs. As in the previous section, we model

such displays as layered compositions of rotated half-wave plates. This model is then used to determine the degree to which multi-layered, single-domain LCDs can be approximated as multi-layer polarization rotators. Third, we characterize multi-layer, multi-domain LCDs. This analysis provides a formal assessment of our prototype, demonstrating, both by theory and experiment, the applicability of a multi-layer polarization rotator approximation.

C.2.1 Multi-Layer Polarization Rotators

The Jones matrix $\mathbf{J}_{\text{R-K}}(\phi_1, \phi_2, \ldots, \phi_K)$, representing a K-layer composition of polarization rotators, is given by

$$\mathbf{J}_{\text{R-K}}(\phi_1, \phi_2, \ldots, \phi_K) = \mathbf{R}(-\phi_K)\,\mathbf{R}(-\phi_{K-1}) \cdots \mathbf{R}(-\phi_1) = \begin{pmatrix} \cos(\sum_{k=1}^{K} \phi_k) & -\sin(\sum_{k=1}^{K} \phi_k) \\ \sin(\sum_{k=1}^{K} \phi_k) & \cos(\sum_{k=1}^{K} \phi_k) \end{pmatrix}, \tag{S.9}$$

where $\{\phi_1, \phi_2, \ldots, \phi_K\}$ are the incremental polarization state rotations induced at each layer. Comparing Equation S.9 to Equation S.1 reveals that layered polarization rotators effectively apply a counterclockwise rotation to the incident polarization state by an angle $\theta = \sum_{k=1}^{K} \phi_k$. This result leads to the following expression for the normalized intensity $I_{\text{R-K}}(\phi_1, \phi_2, \ldots, \phi_K)$ for a K-layer polarization rotator enclosed by closed linear polarizers:

$$I_{\text{R-K}}(\phi_1, \phi_2, \ldots, \phi_K) = I_0 \left| \begin{pmatrix} 0 & 1 \end{pmatrix} \left(\Pi_{k=1}^{K} \mathbf{R}(-\phi_{K-k+1}) \right) \begin{pmatrix} 1 \\ 0 \end{pmatrix} \right|^2 = I_0 \sin^2 \left(\sum_{k=1}^{K} \phi_k \right), \tag{S.10}$$

confirming Equation 5 from the primary text and forming the basis for the tomographic optimization in Section 3.3.

C.2.2 Multi-Layer, Single-Domain LCDs

We model multi-layer, single-domain LCD panels as layered compositions of rotated half-wave plates. The Jones matrix representing a K-layer display of this type is given by

$$\mathbf{J}_{\text{HWP-K}}(\alpha_1, \alpha_2, \ldots, \alpha_K) = \mathbf{J}_{\text{HWP}}(\alpha_K)\,\mathbf{J}_{\text{HWP}}(\alpha_{K-1}) \cdots \mathbf{J}_{\text{HWP}}(\alpha_1) \tag{S.11}$$

$$= \begin{pmatrix} \cos(\sum_{k=1}^{K} (-1)^{k-1} 2\alpha_k) & \sin(\sum_{k=1}^{K} (-1)^{k-1} 2\alpha_k) \\ (-1)^{k-1} \sin(\sum_{k=1}^{K} (-1)^{k-1} 2\alpha_k) & (-1)^{k} \cos(\sum_{k=1}^{K} (-1)^{k-1} 2\alpha_k) \end{pmatrix}, \tag{S.12}$$

where $\{\alpha_1, \alpha_2, \ldots, \alpha_K\}$ are the rotation angles of the liquid crystal directors for each layer. If K is even, such displays operate similarly to layered polarization rotators and effectively apply a clockwise rotation by an angle $\theta = \sum_{k=1}^{K} (-1)^{k-1} 2\alpha_k$. Yet, for any value of $K \geq 1$, the resulting normalized intensity $I_{\text{HWP-K-1}}(\alpha_1, \alpha_1, \ldots, \alpha_K)$ mimics that of multi-layer polarization rotators (i.e., Equation S.10):

$$I_{\text{HWP-K-1}}(\alpha_1, \alpha_1, \ldots, \alpha_K) = I_0 \left| \begin{pmatrix} 0 & 1 \end{pmatrix} \left(\Pi_{k=1}^{K} \mathbf{J}_{\text{HWP}}(\alpha_{K-k+1}) \right) \begin{pmatrix} 1 \\ 0 \end{pmatrix} \right|^2 = I_0 \sin^2 \left(\sum_{k=1}^{K} (-1)^{k-1} 2\alpha_k \right). \tag{S.13}$$

However, unlike layered polarization rotators, every other layer applies a clockwise rotation to the incident polarization state. In practice, one could modify the projection matrix in Equation 6 and the constraints in Equation 7 of the primary text to allow for this discrepancy. Alternatively, as proposed by Moreno et al. [2007], each LCD could be enclosed with additional optical elements (e.g., wave plates) to ensure each layer acts as a polarization rotator. For example, under this model, the addition of a half-wave plate after each panel effectively creates a polarization rotator such that $\mathbf{J}_{\text{HWP}}(0)\,\mathbf{J}_{\text{HWP}}(\alpha) = \mathbf{R}(2\alpha)$. Yet another design alternative is to reverse every other panel such that each layer k effectively applies a counterclockwise rotation by an angle $2\alpha_k$. In summary, whether through optical or computational means, multi-layer, single-domain LCDs can be operated equivalently to layered polarization rotators under this model. It remains to be shown experimentally how well such panels behave in practice since, as we describe in the following section, our prototype uses multi-domain panels.

C.2.3 Multi-Layer, Multi-Domain LCDs

As confirmed in Section C.1.3 and by measurements in Figure S.6, Barco E-2320 PA panels contain multiple domains. As result, we require a multi-layer, multi-domain LCD model to formally assess the deviation of our prototype from the desired layered polarization rotator implementation. We consider each layer k as a rotated half-wave plate containing two domains with opposite liquid crystal director angles (i.e., $\alpha_k^{(1)} = -\alpha_k^{(2)} = \alpha_k$). Consider a two-layer LCD. Any given optical ray passes through one domain in each layer; yet, if one considers the bundle of rays passing through a local region of each layer, then four cases occur, corresponding to the different combinations of domains that can be traversed by each ray. Summing over these combinations yields the following expression for the normalized intensity $I_{\text{HWP-2-2}}(\alpha_1, \alpha_2)$ for a two-layer, two-domain LCD enclosed by crossed linear polarizers.

$$I_{\text{HWP-2-2}}(\alpha_1, \alpha_2) = \frac{I_0}{4} \sum_{i=1}^{2} \sum_{j=1}^{2} \left| \begin{pmatrix} 0 & 1 \end{pmatrix} \mathbf{J}_{\text{HWP}} \left(\alpha_2^{(j)} \right) \mathbf{J}_{\text{HWP}} \left(\alpha_1^{(i)} \right) \begin{pmatrix} 1 \\ 0 \end{pmatrix} \right|^2 \tag{S.14}$$

$$= I_0 \left(\frac{\sin^2(2(\alpha_1 + \alpha_2)) + \sin^2(2(\alpha_1 - \alpha_2))}{2} \right) \tag{S.15}$$

Note that the predicted transmission properties of such displays differ from those predicted for layered polarization rotators (Equation S.10). For rays passing through LCD directors with similar rotation directions (i.e., either both clockwise or both counterclockwise), the emitted intensity will be proportional to $\sin^2(\alpha_1 - \alpha_2)$—consistent with a two-layer, single-domain LCD. For the remaining rays, the emitted intensity will be proportional to $\sin^2(\alpha_1 + \alpha_2)$—consistent with a two-layer polarization rotator. Since these two cases occur with equal frequency, Equation S.15 predicts that two-layer, two-domain LCDs will deviate from the characteristics expected for two-layer polarization rotators (due to the presence of the second term). As discussed in Appendix A of the primary text, Equation S.15 constitutes a *non-linear* image formation model; such models cannot be optimized using the efficient SART algorithm described in Section 3.3. Thus, we conclude that the polarization rotator model, while introducing artifacts in the displayed light field, provides a practical method to achieve real-time display with such panels.

The preceding analysis can be directly extended to four-layer LCDs, yielding the following expression for the normalized intensity $I_{\text{HWP-4-2}}(\alpha_1, \alpha_2, \alpha_3, \alpha_4)$ when enclosing such displays with crossed linear polarizers.

$$I_{\text{HWP-4-2}}(\alpha_1, \alpha_2, \alpha_3, \alpha_4) = \frac{I_0}{16} \sum_{i=1}^{2} \sum_{j=1}^{2} \sum_{k=1}^{2} \sum_{l=1}^{2} \left| \begin{pmatrix} 0 & 1 \end{pmatrix} \mathbf{J}_{\text{HWP}} \left(\alpha_4^{(l)} \right) \mathbf{J}_{\text{HWP}} \left(\alpha_3^{(k)} \right) \mathbf{J}_{\text{HWP}} \left(\alpha_2^{(j)} \right) \mathbf{J}_{\text{HWP}} \left(\alpha_1^{(i)} \right) \begin{pmatrix} 1 \\ 0 \end{pmatrix} \right|^2 \tag{S.16}$$

$$\begin{aligned} = \frac{I_0}{8} \Big[& \sin^2(2(\alpha_1+\alpha_2+\alpha_3+\alpha_4)) + \sin^2(2(-\alpha_1+\alpha_2+\alpha_3+\alpha_4)) + \sin^2(2(\alpha_1-\alpha_2+\alpha_3+\alpha_4)) + \\ & \sin^2(2(\alpha_1+\alpha_2-\alpha_3+\alpha_4)) + \sin^2(2(\alpha_1+\alpha_2+\alpha_3-\alpha_4)) + \sin^2(2(\alpha_1-\alpha_2-\alpha_3+\alpha_4)) + \\ & \sin^2(2(\alpha_1-\alpha_2+\alpha_3-\alpha_4)) + \sin^2(2(\alpha_1+\alpha_2-\alpha_3-\alpha_4)) \Big] \end{aligned} \tag{S.17}$$

As before, it is assumed the domains are symmetrically oriented on each layer (i.e., $\alpha_k^{(1)} = -\alpha_k^{(2)} = \alpha_k$). We note that there are now sixteen cases that arise from traversing each domain across the four layers. From Equation S.12, each case corresponds to either a single polarization rotator or a single polarization pseudo-rotator, with effective rotation angle $\theta = 2(\alpha_1^{(i)} - \alpha_2^{(j)} + \alpha_3^{(k)} - \alpha_4^{(l)})$. Due to the enclosing polarizers, only eight of these cases are distinct, yielding the individual terms in Equation S.17. In practice, each term must be weighted by the likelihood of traversing the corresponding combination of domains (depending on the geometric arrangement and scattering properties of the panels), with Equation S.17 assuming equal weighting. Note that the first term corresponds to the desired multi-layer polarization rotator model (Equation S.10). The remaining terms constitute the artifacts introduced by multi-domain LCD panels, compared to the desired implementation. As shown in Figure S.8, Equation S.17 accurately predicts the artifacts exhibited by the prototype. Similarly, the right-hand side of Figure S.7 compares the four-layer polarization rotator model (Equation S.10) to the four-layer, two-domain model (Equation S.17) for the

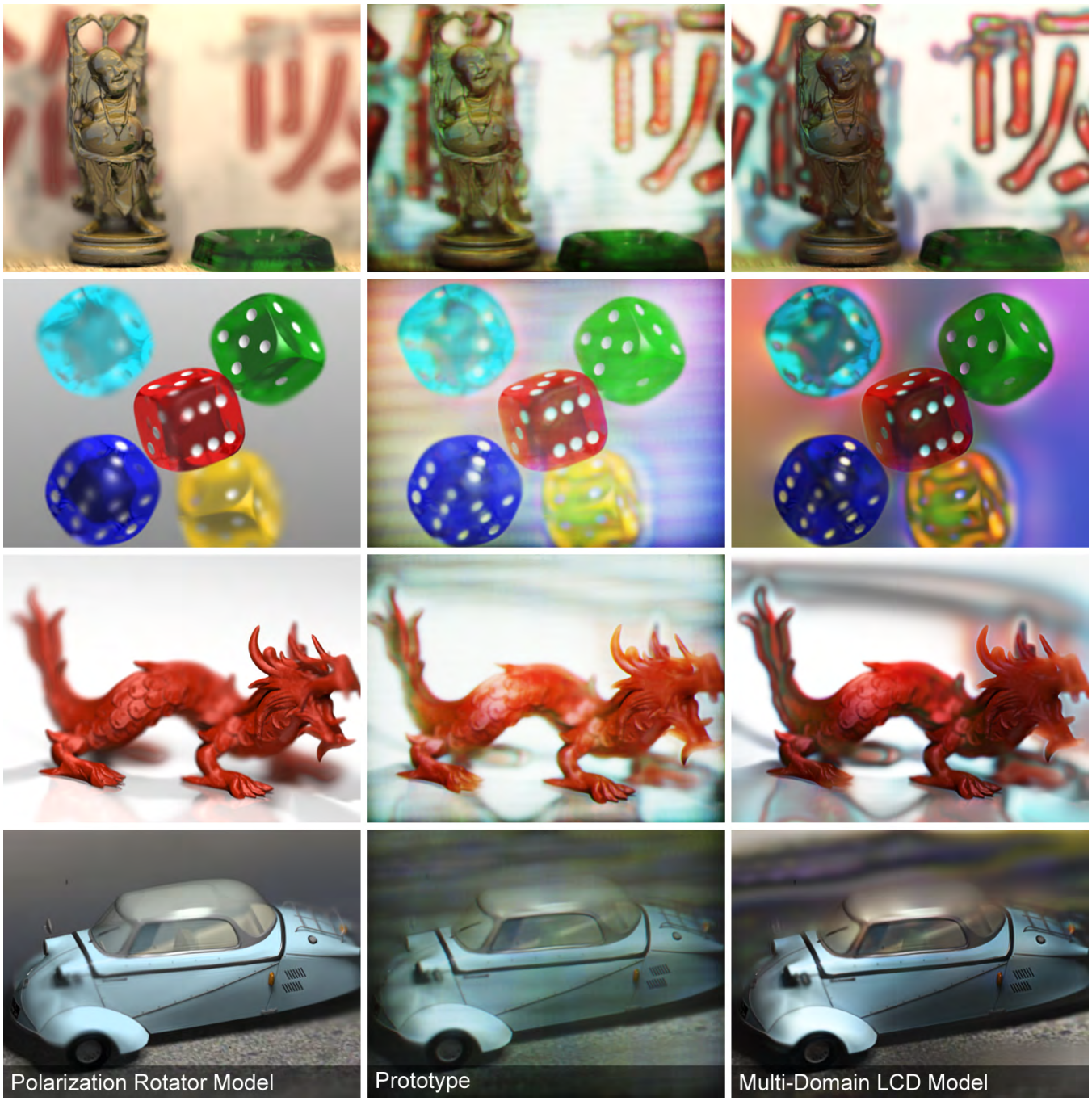

Figure S.8: *Polarization field display using multi-layer LCDs. The central views (i.e., those seen directly in front of the display) are shown for the "Buddha", "dice", "dragon", and "car" scenes. The expected views, as predicted by the layered polarization rotator model and the layered multi-domain LCD model, are shown along the left and right columns, respectively. Corresponding photographs of the prototype are shown along the middle column. Color imagery results from combining three photographs taken while varying the color channel displayed by the monochromatic panels. Note that color artifacts and halos are more accurately predicted by the layered multi-domain LCD model; yet, overall performance is approximated by the layered polarization rotator model. With this approximation, dynamic display is feasible, at the cost of increased image artifacts. See Appendix A of the primary text and Supplementary Appendix C for a detailed assessment of the benefits and limitations of these LCD models.*

case where $\alpha_k = \alpha, \forall k$. In these examples, it is apparent that the multi-domain model more accurately predicts display characteristics than the polarization rotator model. In the following section we assess to what degree the polarization rotator model can be applied to our prototype and to the task of polarization field display in general.

C.3 Discussion

In this supplementary appendix we have applied the Jones calculus for a detailed assessment of the polarization properties of multi-layered LCD panels. As summarized in Figure S.8, this model predicts artifacts exhibited by the prototype, many of which are not as accurately predicted by either the single-domain model or the preferred polarization rotator model. Yet, as demonstrated in the primary text and supplementary video, the prototype achieves dynamic light field display, albeit with artifacts. In this section we conclude, using the presented Jones matrix models, why our prototype succeeds, despite model discrepancies, and propose refinements to mitigate artifacts.

Figure S.7 compares the polarization rotator and multi-domain LCD models to measurements of the prototype. Two important conclusions can be made. First, the multi-domain LCD model more accurately characterizes the performance of the prototype. Second, for small image values (equivalently small effective polarization state rotations), the polarization rotator model correlates well with the observed transmission properties. This insight is reflected by the form of Equation S.17. Only the first term in this expression corresponds to an ideal polarization rotator; the remaining terms are equivalent to layered pseudo-rotators with effective incremental rotations $\phi_k = 2\alpha_k$. We identify two circumstances under which such multi-layer, multi-domain LCDs will behave nearly identically to the desired layered polarization rotator construction. First, if the multi-layer decomposition only produces a significant image value on a single layer, then Equation S.17 reduces to that of a layered polarization rotator (Equation S.10). Second, for dim image regions (i.e., those requiring each layer to display a small image value), the deviation of the multi-domain LCD is minimal; even for bright regions, the intensity remains correlated with the polarization rotator model, often overestimating the brightness (e.g., see the right-hand side of Figure S.7). Thus, as illustrated by the middle column of Figure S.8, prototype artifacts are concentrated in bright image regions—precisely those regions where the polarization rotator approximation deviates most significantly from the multi-domain LCD model.

The preceding analysis explains why the prototype succeeds in displaying light fields. To mitigate remaining artifacts in a practical implementation, one could consider enhancements to the optimization algorithm and to the optical engineering of the panels. We address these issues in turn. We note that the Jones matrix models presented in this supplementary appendix could be used as the foundation for an enhanced optimization procedure. Given that the multi-layer, multi-domain model accurately predicts the appearance of many artifacts observed in the prototype, one would expect its application to lead to improved experimental results. Unfortunately, as discussed in Section 5.2 and Appendix A of the primary text, Equation S.17 constitutes a non-linear image formation model. Thus, the efficient SART algorithm cannot be directly applied. While non-linear optimization procedures could be used, as was considered by Gotoda et al. [2011], such methods do not appear to directly yield a real-time optimization framework. In contrast, our layered polarization rotator model affords dynamic display, but at the cost of requiring specific optical properties for the multi-layer LCD stack. Yet, Moreno et al. [2007] describe practical methods to modify certain LCD panels (i.e., TN variants) using additional quarter-wave plates to implement spatially-controllable polarization rotators. Both computational and optical enhancements remain promising directions for future work, not least of which is to simply replace our multi-domain panels with monochromatic, single-domain alternatives.

In conclusion, the Jones calculus has formally revealed the limitations of the polarization rotator model, as it applies to our prototype. This analysis has uncovered the source of the deviations observed in experiments: our IPS panels contain multiple domains unaccounted for by the proposed model. In practice we have uncovered the circumstances under which a layered polarization rotator model constitutes an accurate approximation. Most significantly, this confirms why experimental results reflect simulations and exposes future directions for eliminating artifacts using a combination of optical and computational refinements. We reiterate the central importance of achieving real-time display in any practical embodiment, with one such approach being exposed in this work: constructing layered polarization rotators amendable to efficient tomographic optimization via the SART algorithm.

D Additional Implementation Details for the Real-Time SART Solver

Although we plan on making our real-time SART implementation publicly available, we outline the general algorithm with pseudocode here. Our implementation, tested on both Windows and Linux, is programmed in C++ and uses OpenGL and Cg shaders. The algorithm assumes a light field with N distinct views and K layers positioned at user-defined depths along the optical axis. Intermediate quantities, including the target light field views and temporary variables storing weights and layer patterns, are internally rendered into 16-bit off-line framebuffers (i.e., Framebuffer Objects, FBOs) before the optimized patterns are displayed on the individual polarization-rotating layers. Only three separate Cg fragment programs are required, each performing the action implied by their names.

Algorithm SART

variables FBO_LF[N], FBO_LF_TMP[N], FBO_LAYERS[K], FBO_W[N], FBO_V[K], DEPTH[K]

function displayLoop()
    if not initialized
        initialize all FBO_W, FBO_V
    end
    drawLightField();
    runSART();
    drawReconstructedLayers();
end

function drawLightField()
    for all light field views i
        activate FBO_LF[i]
        set perspective i
        drawScene(); // render desired 3D scene (e.g., a teapot)
    end
end

function runSART()
    for all iterations k
        // 1. compute $Ax^{(k)}$
        for all light field views i
            activate FBO_LF_TMP[i]
            enable BLEND_MODE
            set perspective i
            for all layers l
                draw 2D plane at DEPTH[l] textured with FBO_LAYERS[l]
            end
        end
        // 2. given $Ax^{(k)}$, compute $W\left(b - Ax^{(k)}\right)$
        for all light field views i
            activate FBO_LF_TMP[i]
            activate CG_SHADER_MULTIPLY_SUBTRACT(FBO_W[i],FBO_LF[i],FBO_LF_TMP[i])
            draw orthographic 2D plane with normalized texcoords
        end
        // 3. given $W\left(b - Ax^{(k)}\right)$, compute $VA^T\left(W\left(b - Ax^{(k)}\right)\right)$
        for all layers l
            activate FBO_LAYER[l]
            activate BLEND_MODE
            for all light field views i
                set projective texture to perspective i
                activate CG_SHADER_MULTIPLY(FBO_V[l],FBO_LAYER[l])
                draw orthographic 2D plane with automatic texcoord generation
            end
        end
        // 4. enforce constraints by clamping values outside feasible range
        for all layers l
            activate FBO_LAYER[l]
            activate CG_SHADER_CLAMP(FBO_LAYER[l])
            draw orthographic 2D plane textured with FBO_LAYER[l]
        end
    end
end

function drawReconstructedLayers()
    for all layers l
        set viewport for display l
        draw orthographic 2D plane textured with FBO_LAYERS[l]
    end
end

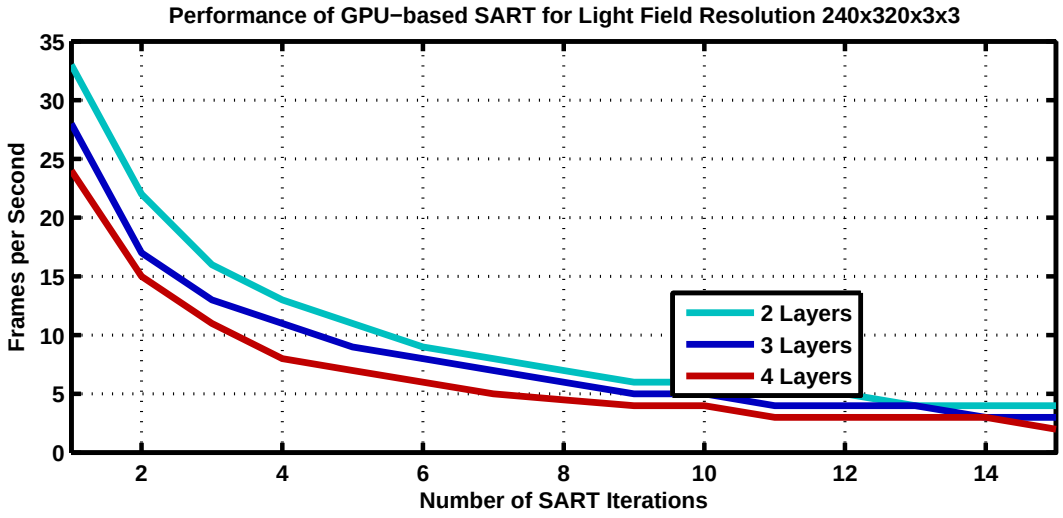

Figure S.9: *Performance of the GPU-based SART implementation as a function of varying numbers of SART iterations (per frame) and varying numbers of polarization-rotating or light-attenuating layers. The light field resolution is* 320×240 *spatial samples and* 3×3 *angular samples; layers have a similar spatial resolution. Timings are measured using the prototype system described in the primary text.*

Supplementary References

COLLETT, E. 2005. *Field Guide to Polarization*. SPIE Field Guides. SPIE Press.

DATE, M., HISAKI, T., TAKADA, H., SUYAMA, S., AND NAKAZAWA, K. 2005. Luminance addition of a stack of multidomain liquid-crystal displays and capability for depth-fused three-dimensional display application. *Applied Optics 44*, 6, 898–905.

GOTODA, H. 2011. Reduction of image blurring in an autostereoscopic multilayer liquid crystal display. In *SPIE Stereoscopic Displays and Applications XXII*, vol. 7863, 1–7.

JONES, R. C. 1941. A new calculus for the treatment of optical systems. *J. Opt. Soc. Am. 31*, 7, 488–493.

MORENO, I., MARTÍNEZ, J. L., AND DAVIS, J. A. 2007. Two-dimensional polarization rotator using a twisted-nematic liquid-crystal display. *Applied Optics 46*, 6, 881–887.

YEH, P., AND GU, C. 2009. *Optics of Liquid Crystal Displays*. John Wiley and Sons.